Ag-Modified ZnO Nanorod Array Fabricated on Polyester Fabric and Its Enhanced Visible-Light Photocatalytic Performance by a Built-in Electric Field and Plasmonic Effect

Hua-Liang Yu,* Ying-Wu Zhou, Xiao-Ling Xue, Li-Qin Liu, Jin-Quan Hong, Zhi-Qun Liu, Hua-Min Chen, Yao-Guo Shen, Biao Zheng, and Jun Wang
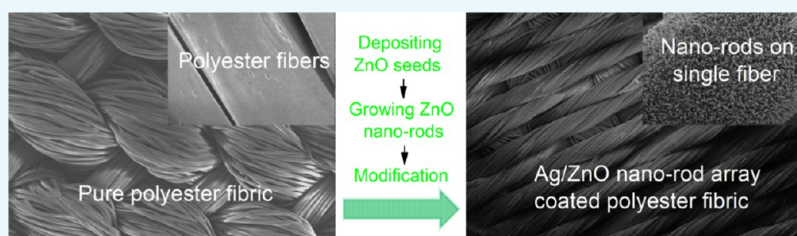
ACCESS | Metrics & More | Article Recommendations

ABSTRACT: ZnO nanorod arrays (NRAs) were fabricated on polyester fabrics (PFs) by a two-step method and modified with Ag by magnetron sputtering. The photogenerated charge transport properties of the Ag/ZnO nanorod heterojunctions were studied by a self-made Kelvin probe system and a surface photovoltage (SPV) test system. The measured work functions (WFs) of the deposited Ag and ZnO nanorod are 4.67 and 5.56 eV, respectively. The SPV spectra indicate that the direction of the inner electric field is from the Ag layer to the inner of the ZnO nanorod. The enhancement of light absorption by the local surface plasma resonance (LSPR) effect of Ag/ZnO NRA was observed by Raman microspectroscopy and UV−vis diffuse reflectance spectroscopy. The photocatalytic activity of the Ag/ZnO NRA-functionalized PFs was evaluated by the photocatalytic degradation of Rhodamine B (RB) solution under visible light. The full photo-oxidation of RB and the outperforming ZnO NRA-coated PFs demonstrate that the enhanced photocatalytic performance of Ag/ZnO NRA-coated PFs results from the cooperation of the inner electric field of the Ag/ZnO nanorod heterojunction and Ag LSPR.

1. INTRODUCTION

With social and economic development, especially the continuous rapid expansion of industrial production all over the world, water pollution has become an increasingly serious worldwide problem. Various pollutants in water have reverse impacts and potential risks on human health and even the whole ecosystem. Therefore, it is urgent to find solutions to the sewage treatment problem. Photocatalysis is an advanced oxidation process and is used to degrade pollutants into H_2O, CO_2, and other non-toxic materials.[1,2] In recent decades, the photocatalytic function of oxide semiconductors has brought about widespread attention to its broader potential for application in the degradation of organic pollutants. Various photocatalysts based on semiconductors such as TiO_2, SnO_2, and ZnO have been widely reported in the recent studies.[3−5] Among them, ZnO is widely employed to deal with organic water pollution issues because of its low cost, extensive source, safety for use, and thermal and photochemical stability.[6,7] However, the fast recombinations of photogenerated electrons and holes in monolayer ZnO decrease the quantum yield greatly, which leads to its poor photocatalytic performance.

Furthermore, ZnO has a wide energy band gap (∼3.2 eV), which limits the absorption spectra to the narrow ultraviolet region. As a result, the ZnO monolayer has rarely been reported as an efficient photocatalyst. In order to overcome the above-mentioned intrinsic weaknesses of ZnO and improve its photocatalytic performance, various strategies, such as the synthesis of nanostructure meterials and formation of heterostructures, utilizing the surface plasma resonance effect, have been adopted.

ZnO-based heterojunctions, in which ZnO couples with another semiconductor[8−10] or precious metal,[11,12] have received wide attention. In a semiconductor−semiconductor heterojunction scheme, the photogenerated charges are separated by the built-in electric field, in which the

photogenerated holes flow along the direction of the built-in electric field, while the photogenerated electrons migrate along the opposite direction of the photogenerated holes. To fabricate such an effective inner electric field to achieve a high photocatalytic activity, the selection of the components of the heterojunction is very important. The difference of the work function (WF) between the coupled semiconductors determines the magnitude and direction of the inner electric field. As a result, experimental investigation into the interface properties of the coupled semiconductors, including the WF measurement of each component, is of great importance. In our previous studies, we have developed the Kelvin probe system and investigated the photoelectric properties of Ag_2O/TiO_2 heterojunctions. The good photocatalytic performance of Ag_2O/TiO_2 was attributed to the large WF difference between the Ag_2O layer and the TiO_2 layer.[13]

In the precious metal–semiconductor heterojunction (Schottky junction) scheme, for a well-designed Schottky junction, there is also an effective inner electric field near the Schottky junction interface, promoting the separation of photogenerated electrons and holes.[11] More importantly, precious metal nanomaterials can greatly enhance the photocatalytic performance of metal oxides due to their local surface plasmon resonance effect, which can extend the range of optical absorption of the coupled metal oxide semiconductor.[14] Deposition of noble metals such as Pt, Au, and Ag on the surface of ZnO has become a key research hotspot because of the effective carrier separation and expansion of the bandwidth of light absorption.[15−17]

Photocatalysts with nanoparticle morphology often have excellent photocatalytic activity due to their large surface area. However, the powder photocatalysts suffer from serious aggregation, which distinctively reduces their effective surface area and restrains the photocatalytic activity. To overcome these drawbacks, various types of low-dimensional ZnO nanomaterials, such as nanorods,[18] tubes,[19] and flowers,[20] have been used as photocatalysts. Photocatalysts based on ordered ZnO nanorod arrays (NRAs), such as Ag/ZnO nanorods/graphene[21] and Ag/ZnO NRAs on Ni foam,[22] which have a high surface area and structural stability, displayed excellent photocatalytic performance in many recent studies. Substrates such as nylon,[23] cotton,[24] polyester,[25] and soda-lime glass,[26] on which the nanorod arrays grow, can prevent the nanorods from aggregation effectively. In addition, by the immobilization of photocatalysts on the substrates, it is easy for photocatalysts to be separated or recycled from the processed solution. Polyester fabrics (PFs) have many advantages such as flexibility, stable chemical properties, and low cost. As flexible synthetic materials, PFs have been used as substrates to grow ZnO nanorod-based solar cells[27] and for antibacterial coating.[28] However, only few studies have reported that PFs acted as substrates for preparation of photocatalysts such as ZnO photocatalytic coating with flake-like structure[29] and Bi_2WO_6/TiO_2 nanorod array coating with self-cleaning function.[30] There are no reports on Ag/ZnO NRA-modified PFs acting as a highly active visible-light photocatalyst. The photocatalytic mechanisms for Ag/ZnO NRA-based photocatalysts also need more reliable experimental verification.

In this work, we reported the successful preparation of ZnO NRA on polyester fabric (PF) by a two-step process and the modification of ZnO NRA by a Ag layer deposited using magnetron sputtering. The photocatalytic experiment results indicate that the Ag/ZnO NRA-modified PF can degrade

Rhodamine B (RB) under visible light efficiently. Furthermore, the mechanisms of the outstanding photocatalytic performance of Ag/ZnO NRA-modified PF were investigated in detail using the Kelvin probe system, surface photovoltage (SPV) test system, Raman microspectroscopy, and UV−vis diffuse reflectance spectroscopy (DRS). The outstanding photocatalytic performance of Ag/ZnO NRA-coated PFs was attributed to the combined effect of the inner electric field of the Ag/ZnO nanorod heterojunction and Ag local surface plasma resonance (LSPR).

2. EXPERIMENTAL DETAILS

2.1. Synthesis of ZnO NRA- and Ag/ZnO NRA-Coated PFs.
The PFs made up of ∼50 μm thick fibers were used as substrates of the photocatalysts. All PF substrates were washed ultrasonically with ethanol for 10 min to clear the impurities from the surfaces of the fibers. ZnO NRA-coated PFs (sample 1) were synthesized via a two-step process. Firstly, the ZnO seed layer was deposited on polyester substrate via radio frequency (RF) reactive magnetron sputtering with a Zn target at room temperature. The sputtering pressure, sputtering power, and Ar/O_2 ratio were 0.6 Pa, 300 W, and 20:10, respectively. The distance from the target to the polyester substrate was set to 12 cm (the same below). The thickness of the ZnO seed layer was ∼150 nm, which was monitored and measured by a film thickness controller (INFICON, SQC 310). In the second step, ZnO NRAs were grown on the seeded polyester fibers by a typical hydrothermal synthesis method. Zinc nitrate hexahydrate and hexamethylenetetramine were added to deionized water under constant stirring to form a water solution of zinc nitrate hexahydrate (100 mM/L) and hexamethylenetetramine (100 mM/L), which was used to grow ZnO NRA. Fifty milliliters of this solution was added to 150 mL of Teflon bottle with a polyester bracket on the bottom. Then, the ZnO-seeded PF was dipped into the solution and laid on the bracket with the ZnO-seeded side facing down. The mixture was agitated at 95 °C for 4 h in a laboratory oven to grow ZnO nanorods. After cooling down naturally, the sample was taken out and washed in deionized water several times and dried at 120 °C in the laboratory oven.

In order to synthesize Ag/ZnO NRA-coated PFs (sample 2), the Ag layer was further deposited on ZnO NRA-coated PF via RF magnetron sputtering with a Ag target at room temperature. The sputtering pressure and sputtering power were 0.6 Pa and 50 W, respectively. The thickness of the Ag film was ∼100 nm. As a comparison, the PF with a 150 nm ZnO seed layer was used as the control sample (sample 3).

2.2. Characterization of ZnO NRA- and Ag/ZnO NRA-Coated PFs.
The surface morphologies of the ZnO NRA- and Ag/ZnO NRA-coated polyester samples were investigated using scanning electron microscope (SEM) photographs recorded on Hitachi S-4800. The crystal structures of ZnO NRA and Ag/ZnO NRA were determined by the X-ray diffraction (XRD) spectrum recorded on a Bruker Axs D 8 system. The chemical state of each element in the samples was explored by X-ray photoelectron spectroscopy (XPS, Simadzu UV-2250). The optical absorbance and UV−vis diffuse reflectance spectroscopy (DRS) of ZnO NRA- and Ag/ZnO NRA-coated polyester samples were analyzed by a Puxi TU1901 spectrophotometer. The motions of the photogenerated charges were studied by surface photovoltage (SPV, Stanford SR830) spectra and photoluminescence (PL, Horiba, Dual UV-NIR) spectra. The self-made Kelvin probe
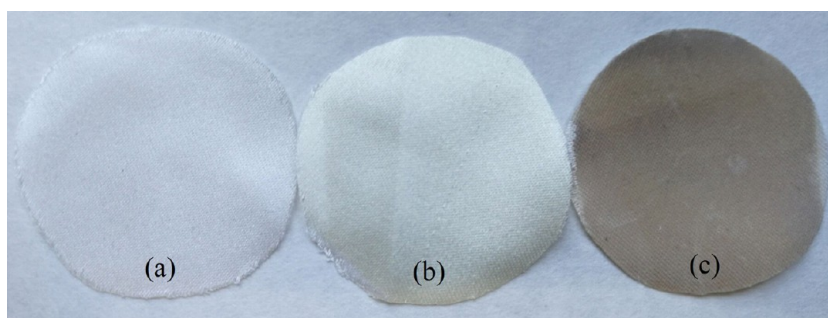
Figure 1. Photographs of (a) pure PF; (b) ZnO nanorod array-coated PF (sample 1); and (c) Ag/ZnO nanorod array-coated PF (sample 2).
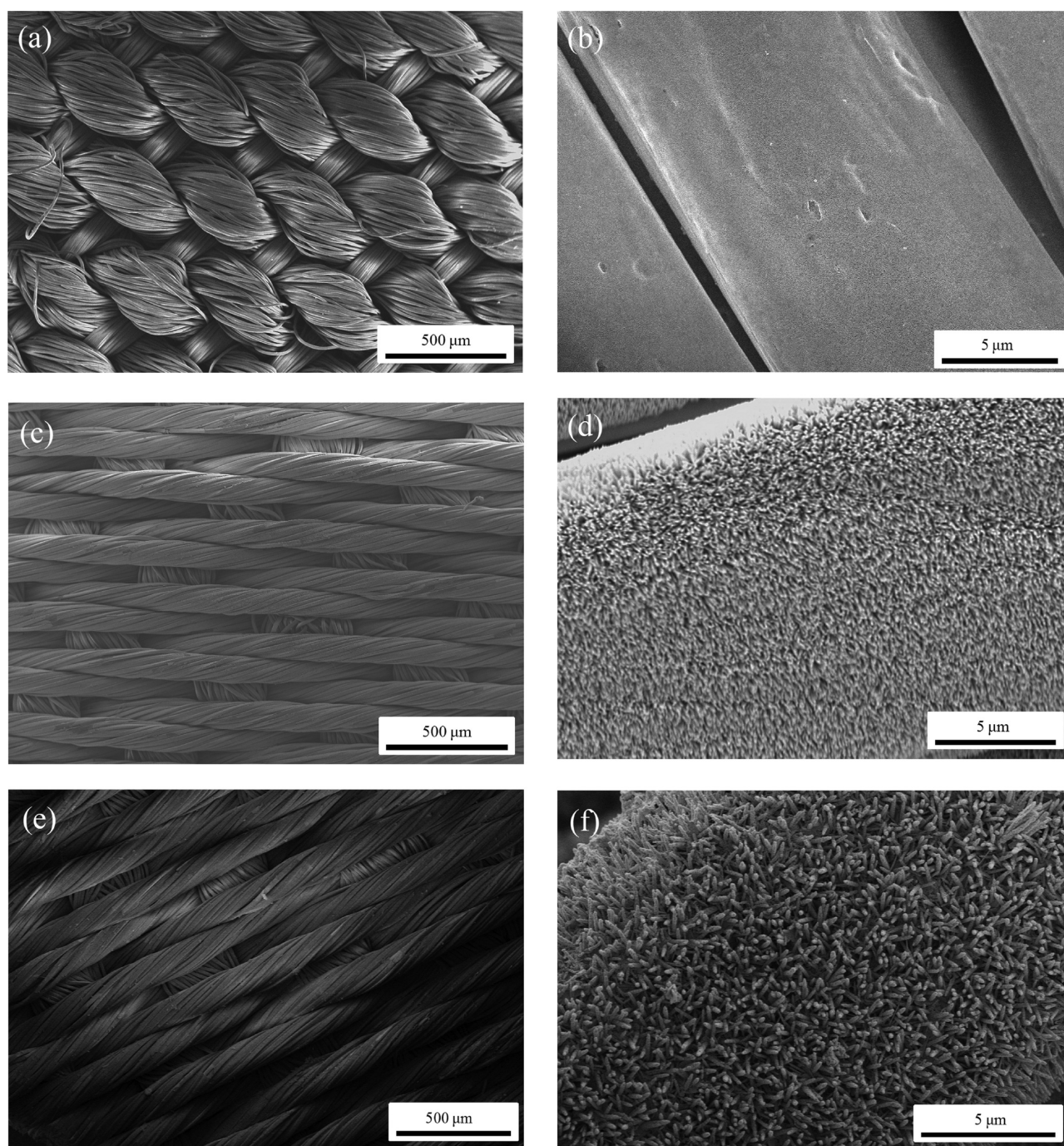
Figure 2. SEM images of (a, b) pure PF; (c, d) ZnO nanorod array-coated PF (sample 1); and (e, f) Ag/ZnO nanorod array-coated PF (sample 2).

system was applied to measure the WFs of ZnO NRA and the deposited Ag layer. Raman spectra of R6G on the samples were measured using a confocal Raman microscope (Horiba T64000).

2.3. Photocatalytic Experiments. In order to evaluate the photocatalytic activities of ZnO NRA- and Ag/ZnO NRA-coated PFs, photocatalytic degradation of RB was performed under visible light. For comparison, all samples were of the same size, which was 45 mm in diameter. The test sample was placed on the bottom of reactor and fixed. 10 mL RB solution with an initial concentration of 5 mg/L as simulated pollutants was poured into the reactor. A 75 W metal halide lamp (Philips 940) coupled with a 420 nm UV cutoff filter was applied as the excitation light source. The optical power density can be adjusted by changing the distance between the photocatalytic reactor and the light source, which was set to 20 mW/cm². The absorbance ratio A/A_0 of RB at the wavelength of 553 nm, which was measured by a UV−vis spectrophotometer (Puxi TU1901) for every 30 min, was selected to evaluate the degradation of RB. The degradation level of RB and the value of photocatalytic rate constant k can be calculated by

$$D(t) = \frac{A_0 - A_t}{A_0} \times 100\% \tag{1}$$

$$-\ln \frac{A_t}{A_0} = k \cdot t \tag{2}$$

where A_0 is the initial absorbance of the RB solution and A_t is the absorbance of the RB solution after photocatalytic degradation for a time interval of t.

3. RESULTS AND DISCUSSION

3.1. Composition and Structure. The optical images of the original PF, ZnO NRA-coated PF, and Ag/ZnO NRA-coated PF are illustrated in Figure 1. ZnO NRA-coated PFs (Figure 1b) show an off-white surface, which is a little different in surface color from that of the pure white original PF (Figure 1a). It is remarkable that the surface of the Ag-modified ZnO NRA (Figure 1c) shows a dark brown color, which is completely different from the metallic luster of the Ag layer deposited on the sites without ZnO NRA, such as the holding trace left in the process of ZnO seed deposition. The morphology of sample 1 observed by SEM shows that ZnO NRA had grown on the surface of the polyester fiber, as shown in Figure 2c,d. For comparison, the SEM image of the original PF is also presented in Figure 2a,b. The average diameter of the nanorods on sample 2, as shown in the SEM images, is a little larger than that on sample 1, because a thin Ag film was deposited on the top of ZnO nanorod.

The XRD spectra of pure PF, PF with the ZnO seed layer, ZnO NRA-coated PF, and Ag/ZnO NRA-coated PF are presented in Figure 3. The large characteristic diffraction peaks of samples located between 20 and 40° are due to the semicrystalline polyester fibers.[31] The broad diffraction peak at 54°, which appears in the X-ray diffraction pattern of each sample, also derives from polyester fibers. The sharp peaks of ZnO NRA-coated PF confirm that the ZnO NRA layer has good crystallinity. The peaks are centered around 30.9, 34.6, 36.4, 47.4, and 62.8°, which correspond to the (100), (002), (101), (102), and (103) crystal planes of ZnO (JCPDS 89−0510), respectively.[32] The strongest peak at 34.6° indicates that the ZnO nanorods grew preferentially along [0001]. The
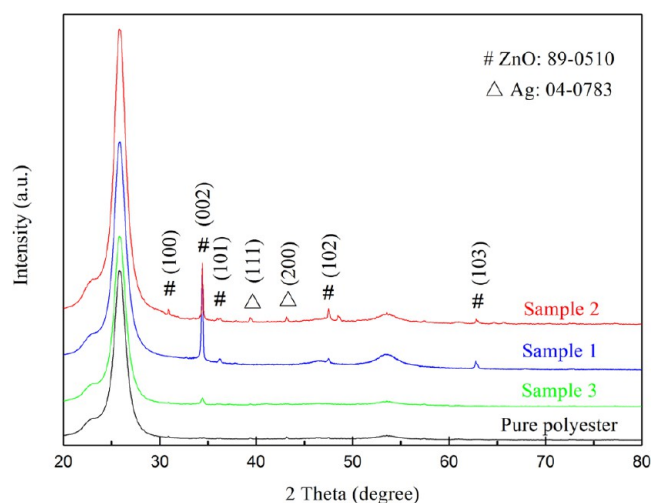

Figure 3. XRD diffraction spectra for pure PF, PF with ZnO seed layer (sample 3), ZnO nanorod array-coated PF (sample 1), and Ag/ZnO nanorod array-coated PF (sample 2).

X-ray diffraction pattern of PF with the ZnO seed layer shows that the (002) peak of ZnO is located at ∼34.6°, which illustrates that the seed deposited by RF reactive magnetron sputtering was ZnO. In the XRD pattern of the Ag/ZnO NRA-coated PF, the peaks positioned at 39.4 and 43.1° can be assigned to the (111) and (200) planes of Ag (JCPDS 04-0783).[33]

The chemical states of Ag and Zn were explored by comparative XPS analysis of the ZnO NRA-coated sample and the Ag/ZnO NRA-coated sample. As shown in Figure 4a,b, the Ag 3d peaks only appeared in the XPS spectrum of the Ag/ZnO NRA-coated sample. The high resolution spectra of the Ag 3d peaks (Figure 4c) show that Ag $3d_{5/2}$ and Ag $3d_{3/2}$ peaks were located at 368.2 and 374.3 eV, respectively, which illustrates the existence of Ag in the metallic state.[34] The Zn 2p spectra (Figure 4d) of sample 1 exhibit two peaks located at 1044.2 and 1021.1 eV, corresponding to the binding energies of Zn $2p_{1/2}$ and Zn $2p_{3/2}$, respectively, and implying a normal state of Zn^{2+} in the ZnO NRA.[35,36]

The UV−vis DRS of the ZnO NRA-coated PF (sample 1) and Ag/ZnO NRA-coated PF (sample 2) are shown in Figure 5. Figure 5a shows that the wavelength range of the light absorbed by the ZnO NRA-coated PF expands from the UV region to visible region, indicating the occurrence of electron transition in the ZnO nanorod between the conduction band and surface states or surface defect states, and between the valence band and surface states or surface defect states, under visible-light irradiation. Both the ZnO NRA-coated PF and Ag/ZnO NRA-coated PF possess a sharp absorption edge at about 400 nm. However, compared with the ZnO NRA-coated PF, the Ag/ZnO NRA-coated PF has increased absorption in both visible and near-ultraviolet light regions, which demonstrates that the Ag layer deposited on ZnO NRA greatly broadens the scope of optical absorption. We speculate that the high absorbance of the Ag/ZnO NRA-composited film can be attributed to the surface plasma resonance of Ag-modified ZnO NRA, which was further investigated by Raman spectra. The band gap of ZnO NRA can be obtained by extrapolating the rising linear part of the plot of $[F(R)h\nu]^2$ versus photon energy to the photon energy axis (the red dotted line in Figure 5b). The band gap of ZnO NRA is determined to be 3.19 eV,
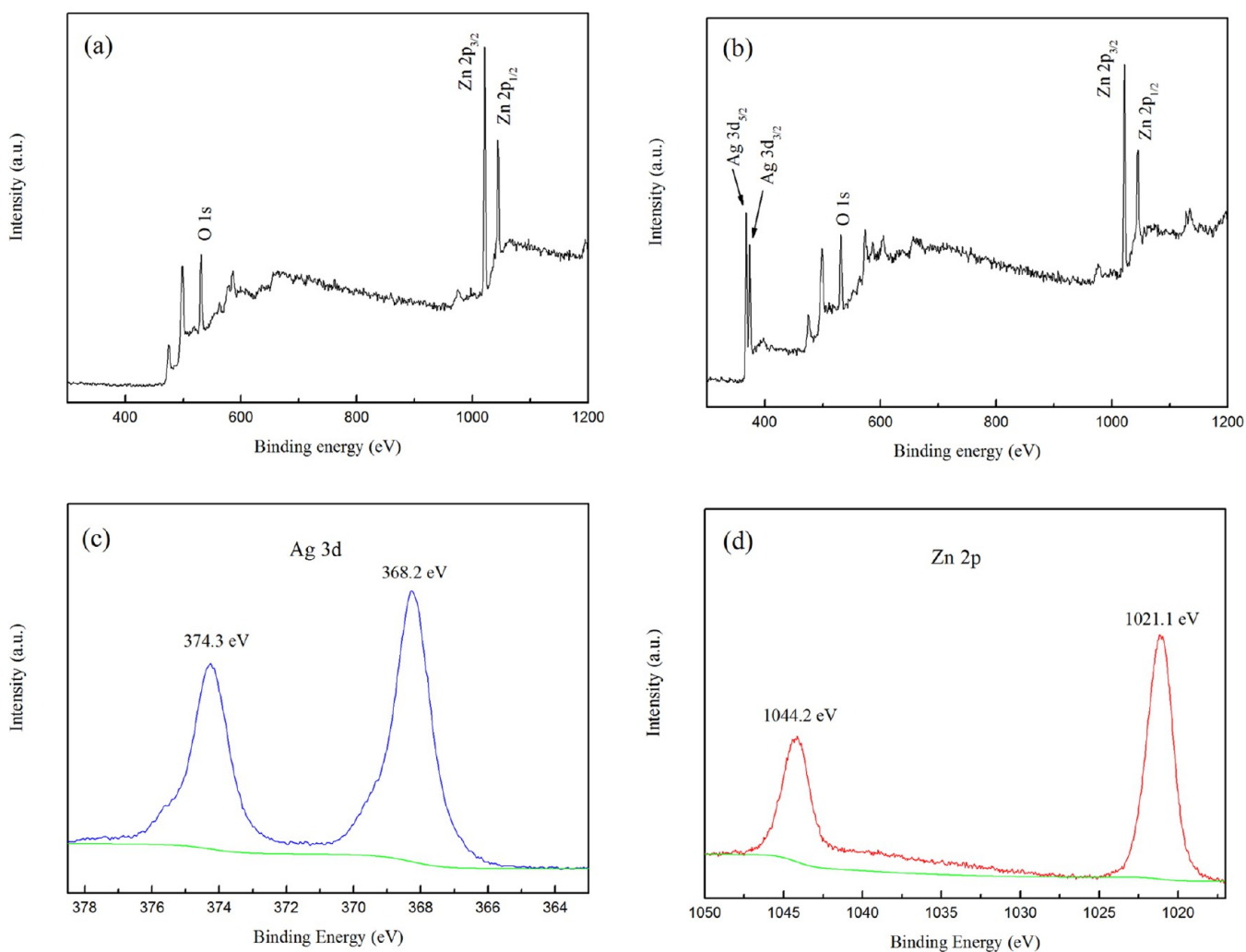
Figure 4. XPS results of the ZnO nanorod array (sample 1) (a) and the Ag/ZnO nanorod array (sample 2) (b). Deconvolution XP spectra of Ag 3d of the Ag/ZnO nanorod array (sample 2) (c) and Zn 2p of the ZnO nanorod array (sample 1) (d).
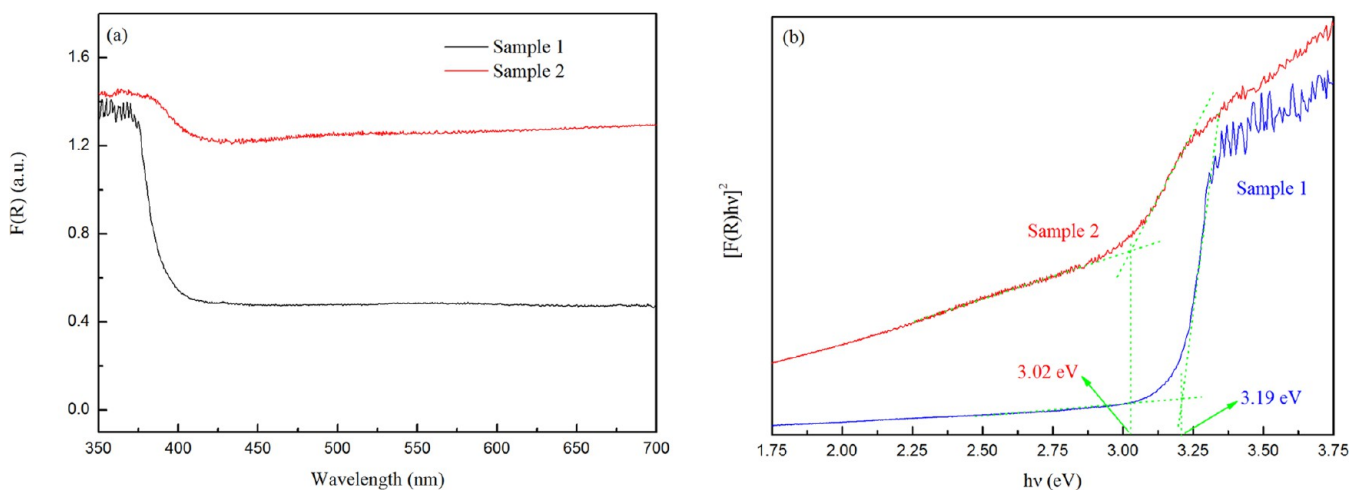

Figure 5. (a) UV−vis diffuse reflection spectra of the ZnO nanorod array (sample 1) and Ag/ZnO nanorod array (sample 2). (b) The corresponding Tauc plot of the samples.

which is in accordance with the reported values in the literature.[11,22]

A micro Raman spectrometer was used to measure the surface enhanced Raman scattering (SERS) of R6G on the PF,

ZnO NRA-coated PF, and Ag/ZnO NRA-coated PF. The concentration of R6G was 10^{-4} M. As shown in Figure 6, intensive Raman signals can be observed in the Raman spectra of the Ag/ZnO NRA-coated PF, indicating that the Ag/ZnO
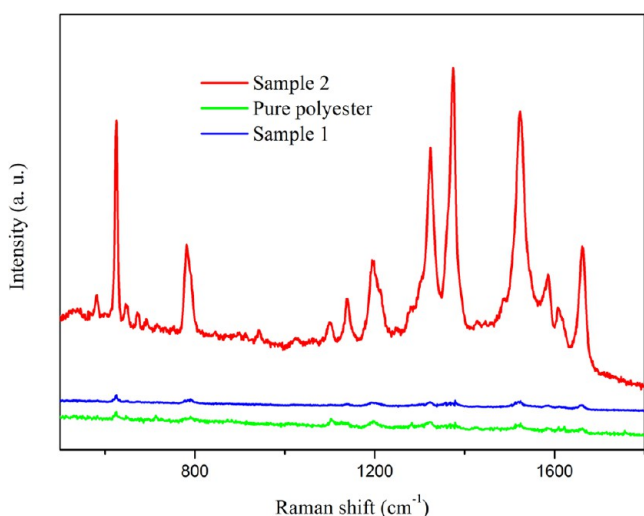
Figure 6. Raman spectra of R6G at a concentration of 10^{-4} M on the ZnO nanorod array-coated PF (sample 1), Ag/ZnO nanorod array-coated PF (sample 2), and pure PF.

NRA-coated PF has high SERS activities. The resolved Raman peaks of R6G, which were located at around 626, 783, 1196, 1324, 1373, 1523, and 1662 cm^{-1}, are in accordance with the previously reported values.[37,38] However, very weak Raman signals were observed on the ZnO NRA-coated PF and pure PF. Because there was no Ag layer on the surface of the ZnO NRA-coated PF and pure PF, both samples cannot produce the SERS effect.

The visible-light photocatalytic performances of the as-prepared ZnO NRA-coated PF and Ag/ZnO NRA-coated PF were evaluated by the photodegradation of RB solution (5 mg/L) under visible light. The degradation curves have been plotted using the absorbance values at 554 nm in the absorbance curves. As shown in Figure 7d,e, even when irradiated by light, the pure PF exhibits extremely weak ability in the elimination of RB. The graphs in Figure 7c,e show that the ZnO-seeded PF has a low photocatalytic activity (40% elimination of RB after 120 min). The ZnO NRA-coated PF shows a remarkably enhanced photocatalytic performance (76% elimination of RB after 120 min), and the Ag/ZnO NRA-coated PF shows the highest photocatalytic performance (90% elimination of RB after 120 min). The pseudo-first-order kinetics of RB degradation are displayed in Figure 7f, in which the first-order kinetics model $\ln(A/A_0) = -kt$ is used to fit the processes of photodegradation. As shown in Figure 7f, the ZnO NRA-coated PF, Ag/ZnO NRA-coated PF, and ZnO-seeded PF have rate constants of 1.18×10^{-2}, 1.85×10^{-2}, and 2.87×10^{-3} min^{-1}, respectively. The quantitative analysis shows the higher photocatalytic activity of sample 2 than sample 1 and sample 3, which implies an obviously enhanced photocatalytic performance of the Ag/ZnO NRA-coated PF.

In order to comprehensively compare the photocatalytic activities of Ag/ZnO NRA and ZnO NRA, we also investigated the photocatalytic performances of samples under UV light (365 nm) with the same optical power density (20 mW/cm^2). The degradations of RB by the Ag/ZnO NRA-coated PF and ZnO NRA coated PF are presented in Figure 8a,b. Both Ag/ZnO NRA-coated PF and ZnO NRA-coated PF showed better photocatalytic activity under UV light irradiation than under visible-light irradiation. The photocatalytic performance of the Ag/ZnO NRA-coated PF (93% elimination of RB after 120

min) was also prominently better than that of the ZnO NRA-coated PF (82% elimination of RB after 120 min) under UV light irradiation, which was similar to the situation under visible-light irradiation.

The photocatalytic performance of Ag/ZnO NRA samples with different thicknesses of the Ag layer under visible-light irradiation were also examined. As shown in Figure 8c,d, Ag/ZnO NRA samples with the 50 nm Ag layer and 100 nm Ag layer exhibited lower photocatalytic activity than that with the 100 nm Ag layer. The photocatalytic activity of the sample with the 50 nm Ag layer was very close to that of the sample with the 100 nm Ag layer (sample 2), which indicated that the optimum thickness of the Ag layer was ∼100 nm.

In order to study the inner electric field and the transport of photogenerated charges in the Ag/ZnO nanorod hetero-junction, the self-made Kelvin probe system, which has been described in detail in the previous article,[13] was employed to measure the WFs of Ag and ZnO NRA. The ZnO NRA and Ag/ZnO NRA were fabricated on an Al foil as the test sample to measure the WFs of ZnO NRA and Ag. Figure 9a shows the measured contact potential difference (CPD) of the Au/Ag and Au/ZnO nanorod arrays, which are 0.430 and −0.456 V, respectively. The WFs of ZnO NRA and Ag can be determined by the following equation: $W_{sample} = W_{Au\,probe} - e \cdot CPD$, where W_{sample} is the WF of the sample, $W_{Au\,probe}$ is the WF of the probe, which is 5.10 eV for the Au probe, and e is the electron charge. The calculated WFs of Ag and ZnO NRA are 4.67 and 5.56 eV, respectively (see Figure 9b). Thus, the E_F difference between Ag and ZnO NRA is 0.89 eV. When the ZnO nanorod integrates with Ag, since the E_F of Ag is higher than that of the ZnO nanorod, electrons migrate from the Ag layer to the ZnO nanorod, and holes transport from the ZnO nanorod to the Ag layer, until the E_F of the ZnO nanorod and Ag are aligned. The transport of electrons and holes results in an inner electric field in the Ag/ZnO nanorod junction. Consequently, the energy bands near the interface between Ag and the ZnO nanorod bend. The direction of the inner electric field in the Ag/ZnO nanorod heterojunction is from the top to the inner of the ZnO nanorod. The inner electric field exerts forces on the photogenerated electron and hole in opposite directions and promotes the separation of photogenerated charges. Specifically, the photogenerated holes drift from the Ag layer side to the inner of the ZnO nanorod and the photogenerated electrons drift in the opposite direction.

According to the above results and the value of the conduction band edge E_{CB} of ZnO reported in the relevant literature studies (the electron affinity of ZnO is ∼4.50 eV),[39,40] the energy band structure diagram of the Ag/ZnO nanorod heterojunction can be obtained and used to illustrate the photocatalytic degradation mechanism of Ag/ZnO NRA. The band structures of ZnO NRA before combining with Ag are shown in Figure 8b. The Fermi levels E_F of Ag and ZnO NRA were 4.67 and 5.56 eV below the vacuum level E_0, respectively. The Fermi level E_F of ZnO NRA is closer to the conduction band edge than the valence band edge, indicating that the as-prepared ZnO NRA is an n-type semiconductor. The band structure of the Ag/ZnO nanorod heterojunction is presented in Figure 9c, in which the direction of the inner electric field is indicated by a vector symbol.

The SPV spectra were further employed to study the transport of the photogenerated charges in the Ag/ZnO nanorod heterojunction. As is known, the SPV spectrum is sensitive to the transfer and separation of photogenerated
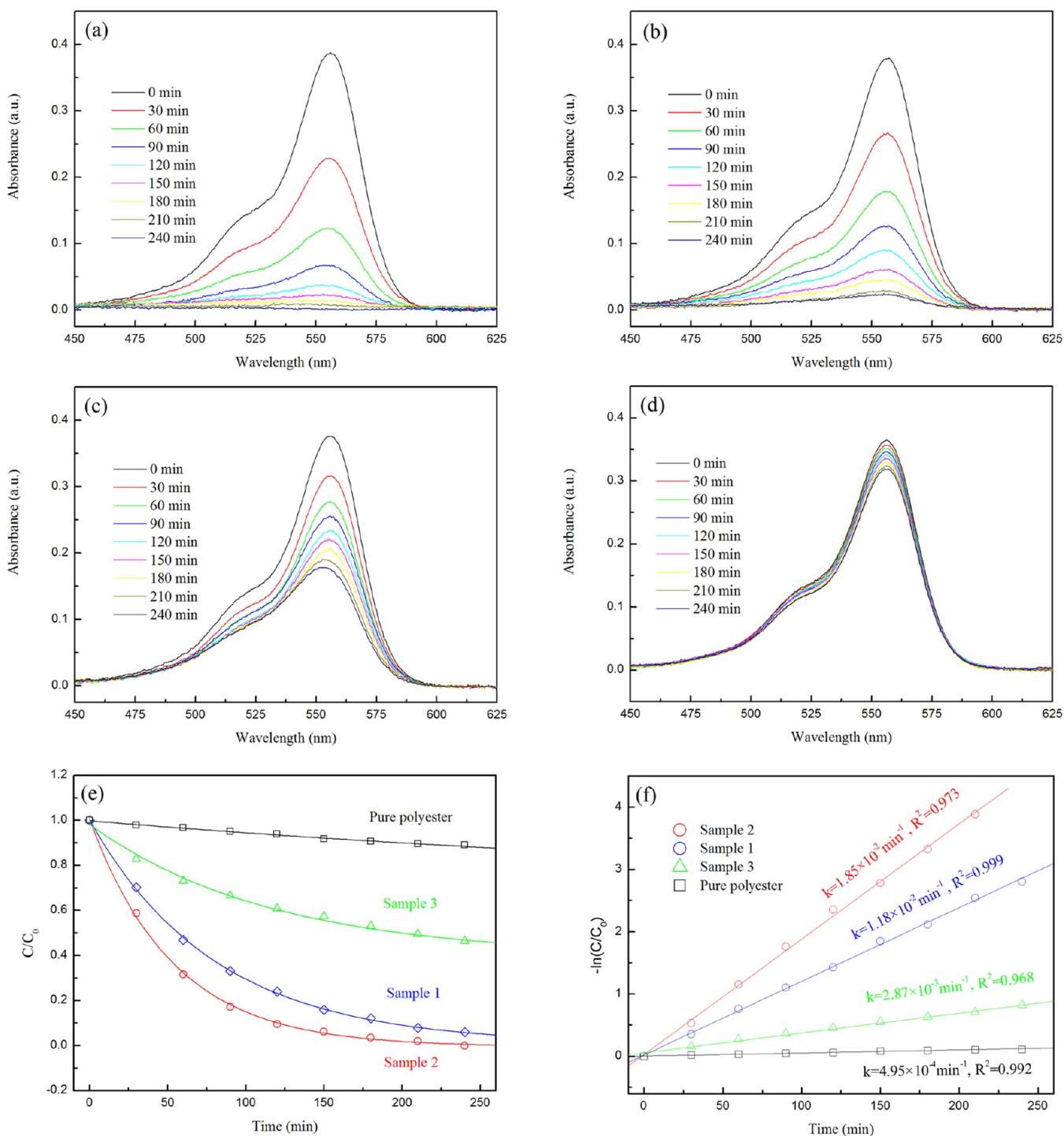
Figure 7. UV−vis absorption spectra of RB (10 mL, 5 mg/L) under visible light (>420 nm) as a function of degradation time in the presence of the (a) Ag/ZnO nanorod array-coated PF; (b) ZnO nanorod array-coated PF; (c) ZnO-seeded PF; (d) initial PF; (e) degradation of RB by Ag/ZnO nanorod array-coated PF, ZnO nanorod array-coated PF, ZnO-seeded PF, and pure PF; (f) plot of $-\ln(C/C_0)$ versus time.

charges. For measuring the SPV signals of the Ag/ZnO nanorod heterojunction, the sandwich structure was fabricated by covering the Ag/ZnO NRA sample with an indium tin oxide (ITO) conductive glass as the counter electrode. At each end of the sample, a piece of insulating tape with the same thickness of ∼100 μm was placed between the sample and the counter electrode to avoid the effect of the ITO film. The measured SPV magnitude spectrum and SPV phase spectrum of the Ag/ZnO NRA sample are shown in Figure 10 and the

inset. An obvious response can be observed from 325 to 550 nm, corresponding to the wavelength range in which the photogenerated charges were generated and separated. It is notable that the SPV response range extends to 550 nm, which is much larger than the absorbing edge of ZnO NRA (∼389 nm) as shown in Figure 5b. The SPV phase angles were in the range between 140 and 180° corresponding to the wavelength range between 325 and 550 nm, indicating that the photogenerated electrons transported to the top of the ZnO
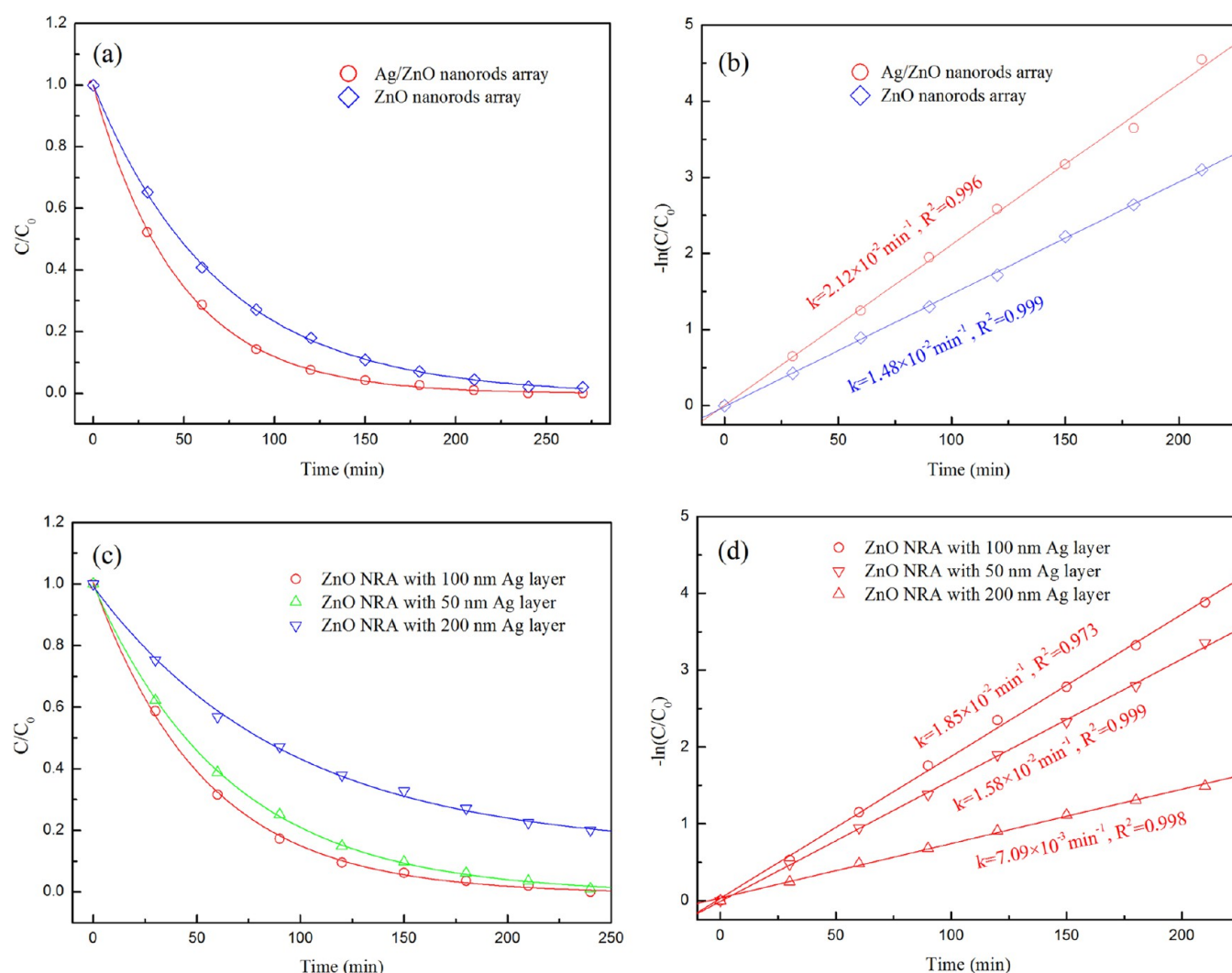
Figure 8. (a) Degradation of RB by ZnO NRA-coated PF (sample 1) and Ag/ZnO NRA-coated PF (sample 2) under UV light irradiation. (b) Kinetic plots for sample 1 and sample 2 under UV light irradiation. (c) Photocatalytic activities for the degradation of RB in the presence of Ag/ZnO NRA-coated PFs with different thicknesses of the Ag layer under visible-light irradiation. (d) Kinetic plots for the Ag/ZnO NRA-coated PF with different thicknesses of the Ag layer under visible-light irradiation.

nanorod and the photogenerated holes migrated to the inner of the ZnO nanorod, which generated a negative SPV response.[41] Therefore, the direction of the inner electric field should be from the Ag layer to the inner of the ZnO nanorod, which is consistent with the conclusion deduced from the measured WF difference between Ag and the ZnO nanorod (Figure 9c). Based on the measured CPD of each component and SPV spectra, we can reach the conclusion that the photogenerated holes and electrons were separated efficiently by the inner electric field in the Ag/ZnO nanorod heterojunction. The Ag layer deposited on the ZnO nanorod plays a critical role in separating the photogenerated charges.

In order to confirm the mechanisms of the photoinduced charge carrier separation, we measured the PL spectra of Ag/ZnO NRA and ZnO NRA samples. PL emission results from the recombination of electron−hole pairs. The larger the intensity of the PL spectra, the higher the electron−hole recombination rate. As shown in Figure 11, Ag/ZnO NRA exhibits a much lower intensity of PL spectra than ZnO NRA, demonstrating that the electron−hole recombination in Ag/ZnO nanorod was greatly suppressed by Ag modification.

To investigate the effect of the built-in electric field in the Ag/ZnO nanorod on the transport of photogenerated electrons and holes, photoelectric current measurements were carried out at a zero bias under UV light (365 nm) irradiation. The carrier separation efficiency can be determined by the intensity of the photoelectric current. The measured photoelectric current spectra of the ZnO NRA sample and Ag/ZnO NRA sample are shown in Figure 12. The Ag/ZnO NRA sample has a photoelectric current of ∼0.2 mA/cm^2, which is ∼3 times higher than that of the ZnO NRA sample. The high photoelectric current can be attributed to the built-in electric field in the Ag/ZnO nanorod heterojunction, which promotes the separation of the photogenerated electrons and holes.
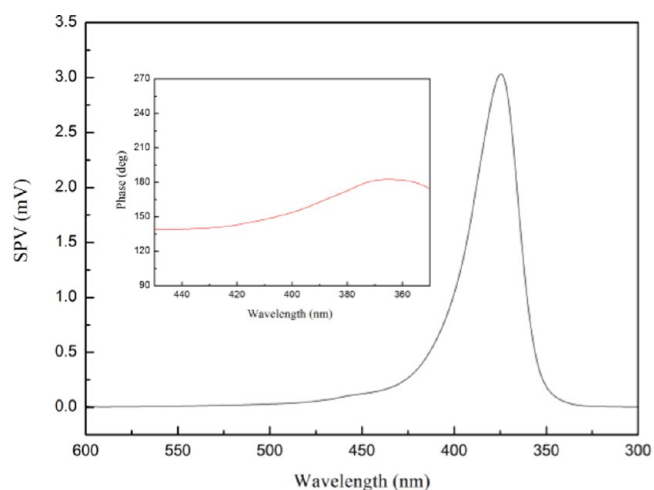
In order to identify the contribution of the active radicals, radical and hole trapping experiments were carried out with various radical scavengers in the photocatalytic degradation process. Disodium ethylenediaminetetraacetic acid (EDTA) (Na$_2$-EDTA), benzoquinone (BQ), and isopropyl alcohol (IPA) were applied to scavenge h$^+$, $\bullet$O$_2^-$, and $\bullet$OH, respectively. Figure 13a shows the effects of BQ, IPA, and Na$_2$-EDTA on the photocatalytic degradation of RB by the Ag/ZnO NRA sample under visible light. The degradation
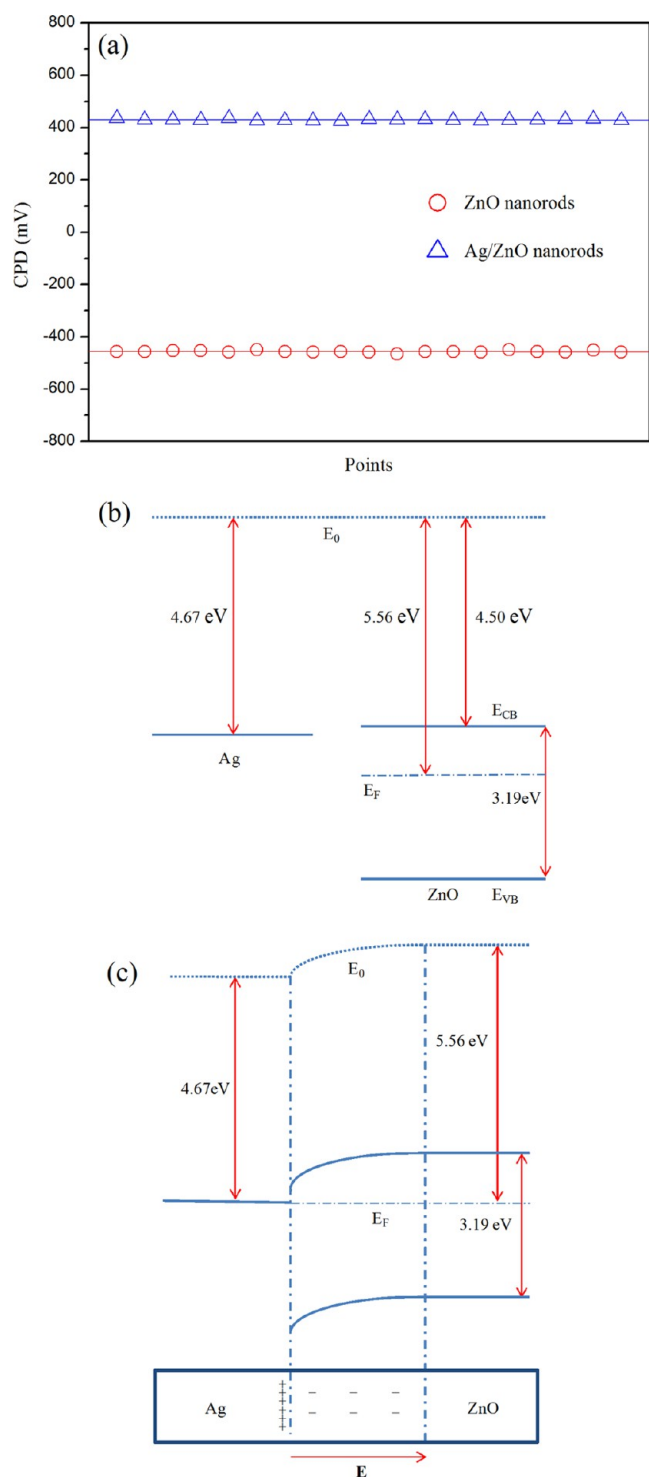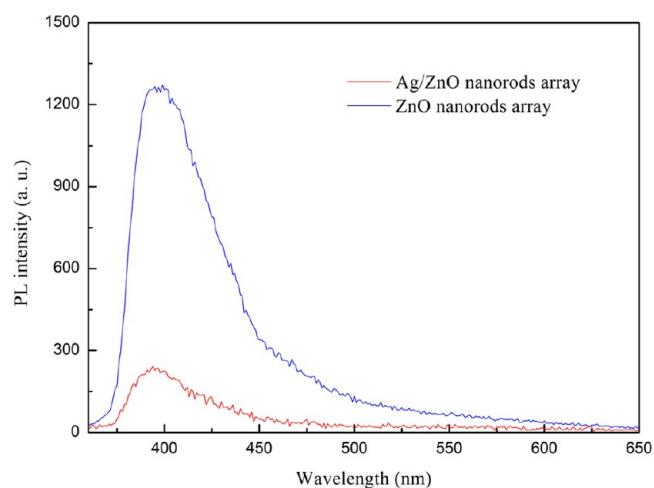
Figure 9. (a) Measured CPDs of the ZnO nanorod array and Ag. (b) Energy band of the isolated ZnO nanorod and Ag. (c) Energy band of the Ag/ZnO nanorod heterojunction.
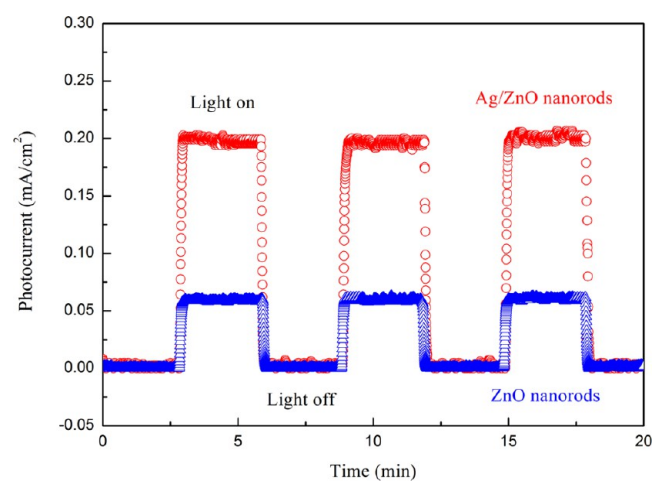

Figure 10. SPV amplitude spectrum and (inset) the SPV phase spectrum of the Ag/ZnO nanorod array.

Figure 11. Photoluminescence (PL) spectra of ZnO NRA (sample 1) and Ag/ZnO NRA (sample 2).

Figure 12. Photocurrent response of ZnO NRA (sample 1) and Ag/ZnO NRA (sample 2).

efficiency of RB only showed a slight decrease after adding IPA, showing that $^\bullet OH$ is not the major living radical in the photodegradation process under the irradiation of visible light. However, when Na$_2$-EDTA and BQ were added as h$^+$ and $^\bullet O_2^-$ scavenger, respectively, an obvious decrease in the photodegradation rate of RB was detected. These results revealed that the photodegradation of RB by Ag/ZnO NRA under visible light can be mainly attributed to h$^+$ and $^\bullet O_2^-$

reactive species. Comparatively, the degradation efficiency of RB after adding BQ decreased a little more significantly than that after adding Na$_2$-EDTA, suggesting that $^\bullet O_2^-$ was a
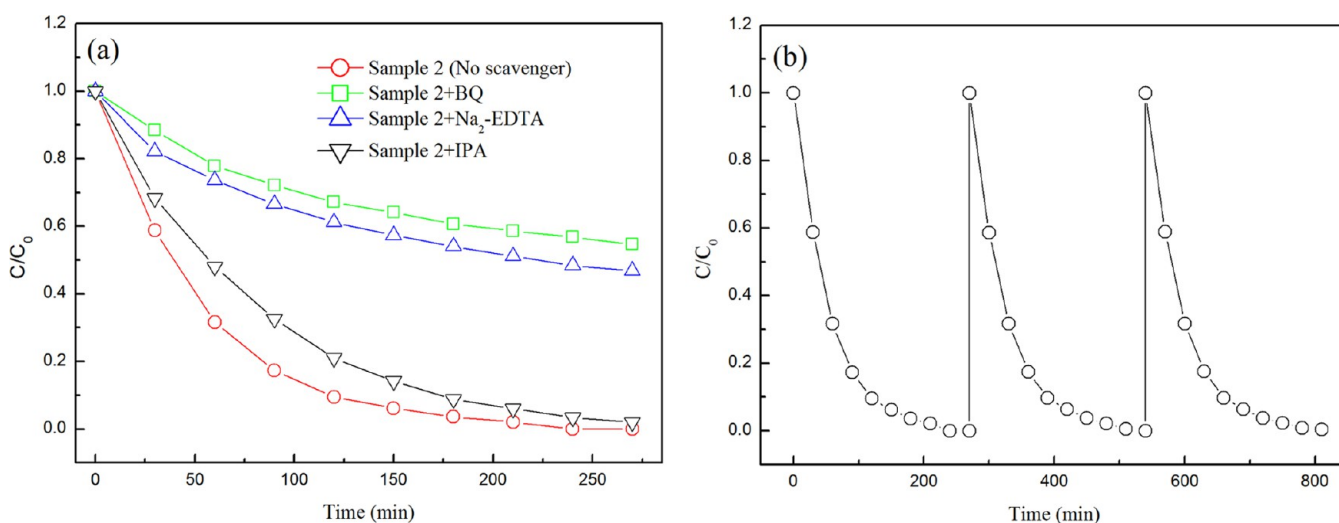
Figure 13. (a) Active species-trapping experiment in the presence of the Ag/ZnO nanorod array-modified PF under visible light. (b) Photocatalytic activity of Ag/ZnO nanorod array-modified PF in different recycling runs.

slightly more important active radical than h^+ in the photodegradation of RB under visible light.

The stability of the photocatalyst is also important for its practical application in removal of pollutants. Figure 13b presents the results of recycling experiments. The degradation efficiency showed no noticeable decrease after three consecutive repeat tests.

4. CONCLUSIONS

ZnO NRA-coated PFs were prepared by a two-step process. The as-prepared ZnO NRA was modified by Ag deposited using magnetron sputtering. The photocatalytic performance of the Ag/ZnO NRA-coated PF is significantly higher than that of the Ag-free ZnO NRA-coated PF. The measured WF difference between Ag and ZnO NRA indicates the existence of an inner electric field in the Ag/ZnO nanorod heterojunction and the direction of the field is from the top to the inner of the ZnO nanorod. The measured SPV spectra demonstrate the efficient separation of photogenerated holes and electrons in the Ag/ZnO nanorod heterojunction, and further confirm the direction of the inner electric field in the Ag/ZnO nanorod heterojunction. The enhancement of light absorption by LSPR effect was observed by UV–vis diffuse reflectance spectroscopy and Raman microspectroscopy. The significantly enhanced photocatalytic activity of the Ag/ZnO NRA-coated PF under visible-light irradiation compared to the Ag-free ZnO NRA-coated PF is attributed to the high photogenerated charges separation efficiency and the enhanced local surface plasma resonance. The as-prepared Ag/ZnO NRA-modified PF can be a good candidate for practical wastewater treatment.

■ AUTHOR INFORMATION

Corresponding Author

Hua-Liang Yu − *Department of Physics and Electronic Information Engineering, Minjiang University, Fuzhou 350108, P. R. China; Fujian Key Laboratory of Functional Marine Sensing Material, Minjiang University, Fuzhou 350108, P. R. China;* ⊙ orcid.org/0000-0003-1171-0596; Email: 2101@mju.edu.cn

Authors

Ying-Wu Zhou − *Department of Physics and Electronic Information Engineering, Minjiang University, Fuzhou 350108, P. R. China; Fujian Key Laboratory of Functional Marine Sensing Material, Minjiang University, Fuzhou 350108, P. R. China*

Xiao-Ling Xue − *Department of Physics and Electronic Information Engineering, Minjiang University, Fuzhou 350108, P. R. China*

Li-Qin Liu − *Department of Physics and Electronic Information Engineering, Minjiang University, Fuzhou 350108, P. R. China*

Jin-Quan Hong − *Department of Physics and Electronic Information Engineering, Minjiang University, Fuzhou 350108, P. R. China*

Zhi-Qun Liu − *Department of Physics and Electronic Information Engineering, Minjiang University, Fuzhou 350108, P. R. China*

Hua-Min Chen − *Department of Physics and Electronic Information Engineering, Minjiang University, Fuzhou 350108, P. R. China; Fujian Key Laboratory of Functional Marine Sensing Material, Minjiang University, Fuzhou 350108, P. R. China*

Yao-Guo Shen − *Department of Physics and Electronic Information Engineering, Minjiang University, Fuzhou 350108, P. R. China; Fujian Key Laboratory of Functional Marine Sensing Material, Minjiang University, Fuzhou 350108, P. R. China*

Biao Zheng − *Department of Physics and Electronic Information Engineering, Minjiang University, Fuzhou 350108, P. R. China; Fujian Key Laboratory of Functional Marine Sensing Material, Minjiang University, Fuzhou 350108, P. R. China*

Jun Wang − *Department of Physics and Electronic Information Engineering, Minjiang University, Fuzhou 350108, P. R. China; Fujian Key Laboratory of Functional Marine Sensing Material, Minjiang University, Fuzhou 350108, P. R. China*

Complete contact information is available at:
https://pubs.acs.org/10.1021/acsomega.1c00460

■ REFERENCES

(1) Cui, Y.; Ma, Q.; Deng, X.; Meng, Q.; Cheng, X.; Xie, M.; Li, X.; Cheng, Q.; Liu, H. Fabrication of Ag-Ag$_2$O/reduced TiO$_2$ nano-photocatalyst and its enhanced visible light driven photocatalytic performance for degradation of diclofenac solution. *Appl. Catal., B* **2017**, *206*, 136−145.

(2) Wang, J.; Xia, Y.; Zhao, H.; Wang, G.; Xiang, L.; Xu, J.; Komarneni, S. Oxygen defectsmediated Z-scheme charge separation in g-C$_3$N$_4$/ZnO photocatalysts for enhanced visible-light degradation of 4-chlorophenol and hydrogen evolution. *Appl. Catal., B* **2017**, *206*, 406−416.

(3) Hu, X. L.; Zhao, H.; Tian, J.; Gao, J. X.; Li, Y. J.; Cui, H. Z. Synthesis of few-layer MoS$_2$ nanosheets-coated TiO$_2$ nanosheets on graphite fibers for enhanced photocatalytic properties. *Sol. Energy Mater. Sol. Cells* **2017**, *172*, 108−116.

(4) Rakibuddin, M.; Ananthakrishnan, R. Fabrication of graphene aerosol hybridized coordination polymer derived CdO/SnO$_2$ heteronanostructure with improved visible light photocatalytic performance. *Sol. Energy Mater. Sol. Cells* **2017**, *162*, 62−71.

(5) Frunza, L.; Diamandescu, L.; Zgura, I.; Frunza, S.; Ganea, C. P.; Negrila, C. C.; Enculescu, M.; Birzu, M. Photocatalytic activity of wool fabrics deposited at low temperature with ZnO or TiO$_2$ nanoparticles: Methylene blue degradation as a test reaction. *Catal. Today* **2018**, *306*, 251−259.

(6) Chouchene, B.; Chaabane, T. B.; Mozet, K.; Girot, E.; Corbel, S.; Balan, L.; Medjahdi, G.; Schneider, R. Porous Al-doped ZnO rods with selective adsorption properties. *Appl. Surf. Sci.* **2017**, *409*, 102−110.

(7) Vaiano, V.; Matarangolo, M.; Murcia, J. J.; Rojas, H.; Navio, J. A.; Hidalgo, M. C. Enhanced photocatalytic removal of phenol from aqueous solutions using ZnO modified with Ag. *Appl. Catal., B* **2018**, *225*, 197−206.

(8) Zhu, L.; Liu, G.; Duan, X.; Zhang, Z. J. A facile wet chemical route to prepare ZnO/TiO$_2$ nanotube composites and their photocatalytic activities. *J. Mater. Res.* **2010**, *25*, 1278−1287.

(9) Xiao, F.-X.; Hung, S.-F.; Tao, H. B.; Miao, J. W.; Yang, H. B.; Liu, B. Spatially branched hierarchical ZnO nanorod-TiO$_2$ nanotube array heterostructures for versatile photocatalytic and photoelectro-catalytic applications: towards intimate integration of 1D-1D hybrid nanostructures. *Nanoscale* **2014**, *6*, 14950−14961.

(10) Ramírez-Ortega, D.; Meléndez, A. M.; Acevedo-Pena, P.; González, I.; Arroyo, R. Semiconducting properties of ZnO/TiO$_2$ composites by electrochemical measurements and their relationship with photocatalytic activity. *Electrochim. Acta* **2014**, *140*, 541−549.

(11) Lee, S. J.; Jung, H. J.; Koutavarapu, R.; Lee, S. H.; Arumugam, M.; Kim, J. H.; Choi, M. Y. ZnO supported Au/Pd bimetallic nanocomposites for plasmon improved photocatalytic activity for methylene blue degradation under visible light irradiation. *Appl. Surf. Sci.* **2019**, *496*, No. 143665.

(12) Chen, F.; Tang, Y.; Liu, C.; Qian, J.; Wu, Z.; Chen, Z. Synthesis of porous structured ZnO/Ag composite fibers with enhanced photocatalytic performance under visible irradiation. *Ceram. Int.* **2017**, *43*, 14525−14528.

(13) Yu, H.-L.; Zhou, Y.-W.; Liu, L.-Q.; Zhang, M.-Y.; Wang, J.-B.; Chen, X.-Y.; Wang, J.; Shen, Y. G.; Zheng, B.; Zhou, B. Simple development of Kelvin probe using a pA meter and its application to study the photocatalytic activities of Ag/TiO$_2$ and Ag$_2$O/TiO$_2$ coated PFs. *Appl. Surf. Sci.* **2021**, *535*, No. 147653-1.

(14) Kriegel, I.; Scotognella, F.; Manna, L. Plasmonic doped semiconductor nanocrystals: Properties, fabrication, applications and perspectives. *Phys. Rep.* **2017**, *674*, 1−52.

(15) He, C.; Cheng, J.; Zhang, X.; Douthwaite, M.; Pattisson, S.; Hao, Z. P. Recent Advances in the Catalytic Oxidation of Volatile Organic Compounds: A Review Based on Pollutant Sorts and Sources. *Chem. Rev.* **2019**, *119*, 4471−4568.

(16) Kim, Y.; Smith, J. G.; Jain, P. K. Harvesting multiple electron-hole pairs generated through plasmonic excitation of Au nanoparticles. *Nat. Chem.* **2018**, *10*, 763−769.

(17) Christopher, P.; Xin, H. L.; Linic, S. Visible-light-enhanced catalytic oxidation reactions on plasmonic silver nanostructures. *Nat. Chem.* **2011**, *3*, 467−472.

(18) Colmenares, J. C.; Kuna, E.; Jakubiak, S.; Michalski, J.; Kurzydłowski, K. Polypropylene nonwoven filter with nanosized ZnO rods: promising hybrid photocatalyst for water purification. *Appl. Catal., B.* **2015**, *170−171*, 273−282.

(19) Jiang, Q.; Liu, Y.; Kan, H.; Yuan, B.; Zhao, H. Microwave-assisted synthesis of hexagonal structure ZnO micro-tubes. *Mater. Lett.* **2012**, *81*, 198−201.

(20) Zhang, G.; Deng, C.; Shi, H.; Zou, B.; Li, Y.; Liu, T.; Wang, W. ZnO/Ag composite nanoflowers as substrates for surface-enhanced Raman scattering. *Appl. Surf. Sci.* **2017**, *402*, 154−160.

(21) Yang, T.-H.; Harn, Y.-W.; Huang, L.-D.; Pan, M.-Y.; Yen, W.-C.; Chen, M.-C.; Lin, C.-C.; Wei, P.-K.; Chueh, Y.-L.; Wu, J.-M. Fully integrated Ag nanoparticles/ZnO nanorods/graphene heterostructured photocatalysts for efficient conversion of solar to chemical energy. *J. Catal.* **2015**, *329*, 167−176.

(22) Zhang, Y. Z.; Liu, L. F.; Van der Bruggen, B.; Leung, M. K. H.; Yang, F. L. A free-standing 3D nano-composite photo-electrode-Ag/ZnO nanorod arrays on Ni foam effectively degrade berberine. *Chem. Eng. J.* **2019**, *373*, 179−191.

(23) Xu, J. H.; Wang, W. Z.; Shang, M.; Sun, S. M.; Ren, J.; Zhang, L. Efficient visible lightinduced degradation of organic contaminants by Bi$_2$WO$_6$ film on SiO$_2$ modified reticular substrate. *Appl. Catal., B* **2010**, *93*, 227−232.

(24) Pakdel, E.; Daoud, W. A.; Sun, L.; Wang, X. G. Visible and UV functionality of TiO$_2$ ternary nanocomposites on cotton. *Appl. Surf. Sci.* **2014**, *321*, 447−456.

(25) Du, Z. F.; Guo, R. H.; Lan, J. W.; Jiang, S. X.; Lin, S. J.; Cheng, C.; Zhao, L. D. Bismuthtungstate coating on PF modified with dopamine for photocatalytic property under visible light irradiation. *Surf. Coat. Technol.* **2017**, *319*, 219−229.

(26) Ratova, M.; West, G. T.; Kelly, P. J. Photocatalytic visible-light active bismuth tungstate coatings deposited by reactive magnetron sputtering. *Vacuum* **2015**, *115*, 66−69.

(27) Wong, C. P.; Mak, C. L. Fabrication and Characterization of ZnO nanorod arrays grown on nickel coated polyester fibbe. *Adv. Mater. Res.* **2012**, *463−464*, 385−393.

(28) Ashraf, M.; Dumont, F.; Campagne, C.; Champagne, P.; Perwuelz, A.; Leriche, A.; Chihib, N.-E. Development of antibacterial PF by growth of ZnO nanorods. *J. Eng. Fibers Fabr.* **2014**, *9*, 15−22.

(29) Du, Z. F.; Cheng, C.; Tan, L.; Lan, J. W.; Jiang, S. X.; Zhao, L. D.; Guo, R. H. Enhanced photocatalytic activity of Bi$_2$WO$_6$/TiO$_2$ composite coated PF under visible light irradiation. *Appl. Surf. Sci.* **2018**, *435*, 626−634.

(30) Ashraf, M.; Champagne, P.; Perwuelz, A.; Campagne, C.; Leriche, A. Photocatalytic solution discoloration and self-cleaning by PF functionalized with ZnO nanorods. *J. Ind. Text.* **2015**, *44*, 884−898.

(31) Harifi, T.; Montazer, M. A robust super-paramagnetic TiO$_2$:Fe$_3$O$_4$:Ag nanocomposite with enhanced photo and bio activities on PF via one step sonosynthesis. *Ultrason. Sonochem.* **2015**, *27*, 543−551.

(32) Park, J. H.; Muralidharan, P.; Kim, D. K. Solvothermally grown ZnO nanorod arrays on (101) and (002) single- and polycrystalline Zn metal substrates. *Mater. Lett.* **2009**, *63*, 1019−1022.

(33) Shao, W. F.; Li, G.; Zhu, P. L.; Zhang, Y.; Ouyang, Q. L.; Sun, R.; Chen, C. H.; Wong, C.-P. Facile synthesis of low temperature sintering Ag nanopaticles for printed flexible electronics. *J. Mater. Sci.: Mater. Electron.* **2018**, *29*, 4432−4440.

(34) Sarkar, D.; Ghosh, C. K.; Mukherjee, S.; Chattopadhyay, K. K. Three dimensional Ag_2O/TiO_2 type-II (p−n) nanoheterojunctions for superior photocatalytic activity. *ACS Appl. Mater. Interfaces* **2013**, *5*, 331−337.

(35) Ou, M.; Wan, S.; Zhong, Q.; Zhang, S.; Song, Y.; Guo, L.; Cai, W.; Xu, Y. Hierarchical Zscheme photocatalyst of g-C_3N_4@Ag/$BiVO_4$ (040) with enhanced visible-light-induced photocatalytic oxidation performance. *Appl. Catal., B* **2018**, *221*, 97−107.

(36) Huang, M. H.; Mao, S.; Feick, H.; Yan, H.; Wu, Y.; Kind, H.; Weber, E.; Russo, R.; Yang, P. Room-temperature ultraviolet nanowire nanolasers. *Science* **2001**, *292*, 1897−1899.

(37) Zang, Y. S.; Yin, J.; He, X.; Yue, C.; Wu, Z. M.; Li, J.; Kang, J. Y. Plasmonic-enhanced self-cleaning activity on asymmetric Ag/ZnO surface-enhanced Raman scattering substrates under UV and visible light irradiation. *J. Mater. Chem. A* **2014**, *2*, 7747−7753.

(38) Michaels, A. M.; Nirmal, M.; Brus, L. E. Surface Enhanced Raman Spectroscopy of Individual Rhodamine 6G Molecules on Large Ag Nanocrystals. *J. Am. Chem. Soc.* **1999**, *121*, 9932−9939.

(39) Wang, Z. L.; Song, J. H. Piezoelectric nanogenerators based on zinc oxide nanowire arrays. *Science* **2006**, *312*, 242−246.

(40) Yin, J.; Yue, C.; Zang, Y. S.; Chiu, C. H.; Li, J. C.; Kuo, H. C.; Wu, Z. H.; Li, J.; Fang, Y. Y.; Chen, C. Q. Effect of the surface-plasmon-exciton coupling and charge transfer process on the photoluminescence of metal-semiconductor nanostructures. *Nanoscale* **2013**, *5*, 4436−4442.

(41) Ivanov, T.; Donchev, V.; Germanova, K.; Kirilov, K. A vector model for analysing the surface photovoltage amplitude and phase spectra applied to complicated nanostructures. *J. Phys. D: Appl. Phys.* **2009**, *42*, No. 135302.